

A model-tested North Atlantic Oscillation reconstruction for the past millennium

Pablo Ortega^{1†}, Flavio Lehner^{2,3†}, Didier Swingedouw⁴, Valerie Masson-Delmotte¹, Christoph C. Raible^{2,3}, Mathieu Casado¹ & Pascal Yiou¹

The North Atlantic Oscillation (NAO) is the major source of variability in winter atmospheric circulation in the Northern Hemisphere, with large impacts on temperature, precipitation and storm tracks¹, and therefore also on strategic sectors such as insurance², renewable energy production³, crop yields⁴ and water management⁵. Recent developments in dynamical methods offer promise to improve seasonal NAO predictions⁶, but assessing potential predictability on multi-annual timescales requires documentation of past low-frequency variability in the NAO. A recent bi-proxy NAO reconstruction⁷ spanning the past millennium suggested that long-lasting positive NAO conditions were established during medieval times, explaining the particularly warm conditions in Europe during this period; however, these conclusions are debated. Here, we present a yearly NAO reconstruction for the past millennium, based on an initial selection of 48 annually resolved proxy records distributed around the Atlantic Ocean and built through an ensemble of multivariate regressions. We validate the approach in six past-millennium climate simulations, and show that our reconstruction outperforms the bi-proxy index. The final reconstruction shows no persistent positive NAO during the medieval period, but suggests that positive phases were dominant during the thirteenth and fourteenth centuries. The reconstruction also reveals that a positive NAO emerges two years after strong volcanic eruptions, consistent with results obtained from models and satellite observations for the Mt Pinatubo eruption in the Philippines^{8,9}.

In the North Atlantic sector, roughly half of the interannual variability in winter atmospheric pressure is explained by fluctuations in the NAO. The NAO is characterized by a changing dipole of sea-level pressure between the Azores and Iceland, and has widespread impacts on temperature and precipitation across Eurasia, North Africa, Greenland and northern North America¹⁰.

A recent study discarded the idea that there has been a strong direct radiative influence of solar forcing on Northern Hemisphere temperatures in the past millennium¹¹. Consequently, the hypothesis has emerged that changes in the NAO could explain part of the decadal-to-centennial variations in these temperatures. Also, NAO variability itself can be externally driven, and therefore allow for an indirect effect of external forcing on temperature not accounted for in the previous study¹¹.

A millennial bi-proxy NAO reconstruction⁷ (hereafter NAO_{Trouet}) shows persistent positive phases during the Medieval Climate Anomaly (MCA, roughly AD 1000–1300; ref. 12), as does a multi-millennial NAO reconstruction from one lake sediment record in Greenland¹³. Other proxy records from the Iberian Peninsula¹⁴ support drier conditions during this period, a common fingerprint of positive NAO phases. However, some doubts have been raised regarding the persistence of a positive NAO phase during medieval times. For example, such persistent phases are not reproduced in any of 13 different past-millennium climate simulations¹⁵. Also, if the NAO

were predominantly positive during this period, low temperatures should be recorded in southwest Greenland¹⁶, and warm temperatures in northwestern Europe, but no indication of such anomalies appears in ice-core records and documentary sources¹⁷. Proxy-based NAO reconstructions are challenging because of the nonstationarity of the statistical relationships and regional teleconnections on which they are based^{18,19}. Moreover, a ‘perfect-model’ study, using reanalyses and climate models as physically consistent surrogates of the real world (see Methods), has shown that the two proxy records involved in NAO_{Trouet} are insufficient to guarantee a robust reconstruction throughout the entire last millennium²⁰.

All of these factors point towards the need for a new multi-proxy NAO reconstruction for the past millennium, based on a larger set of proxy records that is representative of several NAO fingerprints in temperature, precipitation and droughts. Unlike NAO_{Trouet}, which is based on 30-year smoothed data, our reconstruction is built at annual resolution, allowing us to test the effect of major volcanic eruptions and the 11-year solar cycle on the NAO. Although it is well established that a positive NAO-like sea-level pressure pattern is observed one to two years after major volcanic eruptions, most analyses focus on the Pinatubo eruption^{8,9} (the only major eruption to be observed by satellite). The effect of solar activity is less well constrained, although recent studies suggest that the Arctic Oscillation (which is closely linked to the NAO) is modulated by the 11-year solar cycle^{21,22}.

Our study is based on 48 annually resolved proxy time series (Fig. 1a and Extended Data Table 1), which are significantly correlated (P value <0.10) with the longest instrumental record of the NAO (hereafter NAO_{Vinther}²³) in the period in which they overlap. All of these records were screened to fulfil two additional conditions: first, they encompass the eleventh to the twentieth centuries continuously; and second, they have a documented relationship in previous literature with a climate variable easily extractable from climate models.

The NAO is reconstructed using principal component regression (PCR), following the procedure of a previous reconstruction from AD 1400 onwards²⁴ (see Methods). To identify the robust features in the reconstruction, we generate an ensemble that explores the sensitivity to calibration, by extracting 100 random samples of 117 years from the period that is common to all proxies and the NAO (that is, AD 1823–1969). The remaining 30 years will later be used for validation.

Two different alternative ensemble reconstructions are constructed by imposing restrictions on the initial proxy data set. The first ensemble (NAO_{cc}, for ‘calibration-constrained’) uses as many proxy records as possible to guarantee an optimal calibration, verifying first that the proxy records still correlate significantly with NAO_{Vinther} within the calibration period. Figure 1b illustrates the individual contribution (as cumulated weights; see Methods) of the proxy records to the NAO_{cc} reconstruction. Each record participates at least once in the ensemble. This approach optimizes the statistical match with the

¹LSCE/IPSL, UMR 8212 (CEA-CNRS-UVSQ), CEA Saclay, Gif-sur-Yvette 91191, France. ²Climate and Environmental Physics, Physics Institute, University of Bern, Sidlerstrasse 5, 3012 Bern, Switzerland.
³Oeschger Centre for Climate Change Research, University of Bern, Sidlerstrasse 5, 3012 Bern, Switzerland. ⁴EPOC, Université Bordeaux 1, Allée Geoffroy Saint-Hilaire, Pessac 33615, France.

†Present addresses: NCAS Climate, Department of Meteorology, University of Reading, Reading RG6 6BB, UK (P.O.); National Center for Atmospheric Research, 1850 Table Mesa Drive, Boulder, Colorado 80305, USA (F.L.).

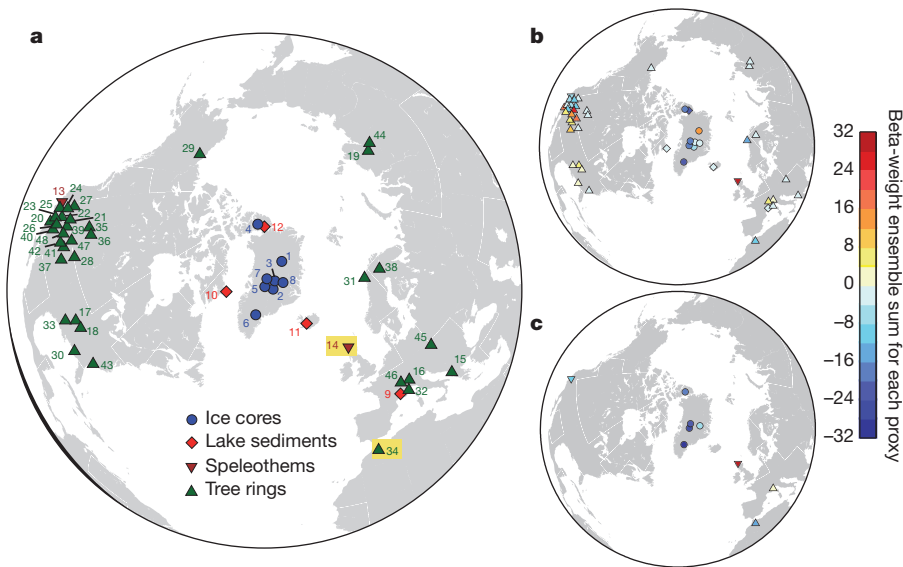


Figure 1 | Proxy selection. **a**, Location of the initial 48 proxy records (ice cores, lake sediments, speleothems or tree rings) preselected for the reconstructions, using symbols and colours to represent the different types of archive. Some symbols have been slightly displaced to improve their visibility. The two proxies used in NAO_{Trouet} are highlighted with yellow boxes. The true coordinates of each record are detailed in Extended Data Table 1. **b, c**, The colours of the symbols now represent the cumulated beta-weights (see Methods) associated with the proxies that contribute to the NAO_{cc} (**b**) and NAO_{mc} (**c**) ensemble reconstructions.

instrumental NAO_{Vinther} within the calibration period, but cannot ensure that NAO-proxy relationships have an actual physical basis, or that these relationships are stationary in time. Both issues are tackled simultaneously in a second ensemble reconstruction (NAO_{mc} for ‘model-constrained’). The proxy selection is first narrowed down with reanalyses (Extended Data Table 2) to guarantee realistic NAO teleconnections, and further constrained with eight past-millennium PMIP3 simulations (Paleoclimate Modelling Intercomparison Project Phase 3; Extended Data Table 3). This latter step ensures that the teleconnections are stable throughout the whole period. The NAO_{mc} ensemble reconstruction uses those proxies whose NAO-climate fingerprint is supported by at least one of the reanalyses and by half of the PMIP3 simulations. This final approach is highly restrictive and leads to a selection of only nine proxy records (Fig. 1c). If some teleconnections are unresolved by models, this method may discard proxy records that are actually sensitive to the NAO.

The two ensemble reconstructions are displayed in Fig. 2a and b and compared to NAO_{Trouet} with 50-year moving correlations (Fig. 2c). Only NAO_{mc} shows some periods of relatively good agreement with NAO_{Trouet} outside the instrumental period, coinciding with the largest-amplitude changes. However, none of the ensemble reconstructions exhibits persistent positive NAO phases in medieval times. Instead, a Student’s *t*-test on their means, applied in 100-year intervals, highlights a first period with non-zero mean negative values that is common to NAO_{mc} and NAO_{Trouet} (left-hand cyan horizontal bar in Fig. 2b). In AD 1150, the NAO_{mc} undergoes a rapid transition towards positive phases, which remain significantly different ($P < 0.05$) from zero for about 240 years (magenta horizontal bar). In the following four centuries, until the industrial period, the NAO_{mc} again depicts predominantly negative values. Similar features, albeit with differences in the timing of phase changes, are found in the NAO_{cc} (Fig. 2a).

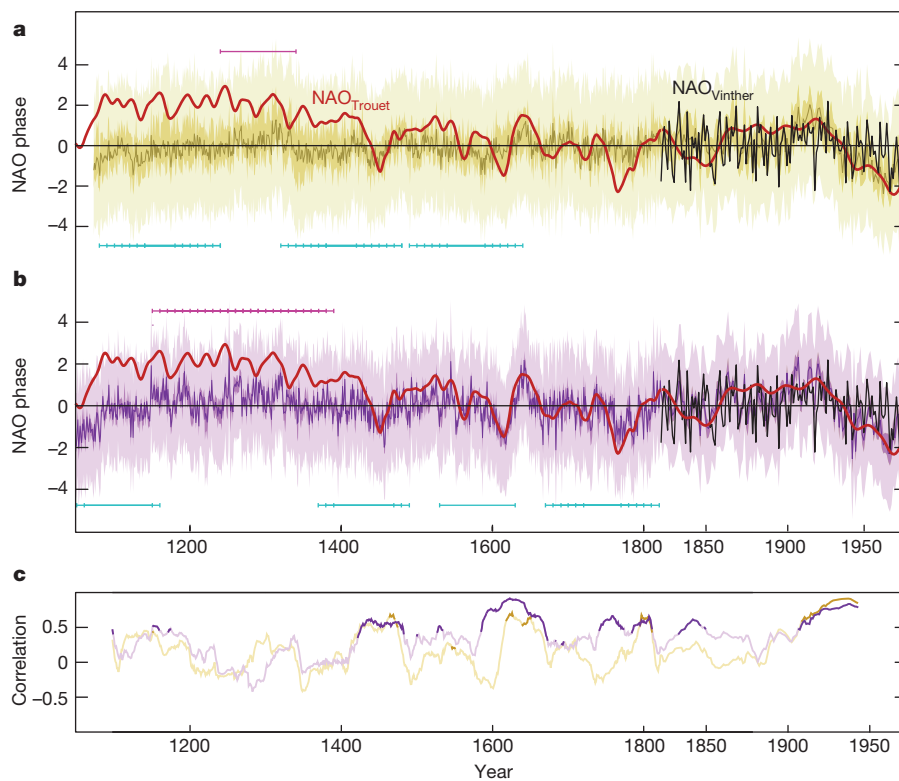


Figure 2 | Ensemble NAO reconstructions. **a**, Ensemble of 100 yearly NAO_{cc} reconstructions. The intermediate and light yellow envelopes represent, respectively, the total ensemble spread, and the regression uncertainties across the ensemble (as departures of ± 2 standard error, s.e., from the individual reconstructions). Also shown are the ensemble mean (dark yellow line), NAO_{Vinther}²³ (black) and NAO_{Trouet}⁷ (red). Horizontal magenta (or cyan) bars enclose centuries (marked by tick marks) with positive (or negative) mean NAO values that are significantly different ($P < 0.05$) than zero (see Methods). **b**, NAO_{mc} ensemble. **c**, 50-year running correlations between the mean ensemble reconstructions and NAO_{Trouet}. Dark-coloured lines represent correlations significant at the 95% confidence level ($P < 0.05$).

We now assess the difference in performance between the ensembles. By construction, NAO_{cc} exhibits higher correlations with $\text{NAO}_{\text{Vintner}}$ within the calibration period than does NAO_{mc} (Fig. 3a), as NAO_{cc} includes more proxy data, and therefore more principal components contribute to the multivariate regression (Extended Data Table 4). However, this does not translate into larger correlations for the validation years (Fig. 3b). Indeed, NAO_{cc} is statistically overfitted with spurious predictors, as shown by the higher validation scores for NAO_{mc} . In Figure 3c–i we verify that both ensemble reconstructions are consistent with other observational and reconstructed NAO time series (see also Extended Data Table 5). Once again, NAO_{mc} stands out, yielding generally higher correlation coefficients with the set of NAO records. We also emphasize the overall good performance of the ensemble mean, with correlations being almost systematically above the median of the ensemble. The contribution of each proxy is estimated as the total sum of its beta-weights. In both ensemble reconstructions, and most prominently in NAO_{mc} , the largest weights correspond to south and west Greenland ice cores (where the strongest impacts of the NAO have been reported^{15,16}) and to the speleothem from Scotland (Fig. 1b, c).

To test the reliability of the NAO_{mc} reconstruction outside the observational period, we perform a perfect-model analysis of the PMIP3 simulations. We reproduce the same PCR strategy now applied to pseudo-proxies extracted from model outputs and perturbed with noise to mimic the actual proxies (Methods; ref. 25). To be more faithful to the original reconstruction, we use only the six PMIP3 simulations that represent a stable relationship of the NAO with the nine proxies in Fig. 1c. Extended Data Fig. 1 represents the correlation of the ensemble NAO_{mc} pseudo-reconstruction with the simulated NAO in three different periods: the same two subsets used before for calibration/validation, and the long validation period AD 1000–1822. As in the actual reconstructions (Fig. 3), all models depict a notably large spread for the 30-year validation scores, estimated with fewer degrees of freedom and therefore being more sensitive to stochastic noise than are the calibration statistics. In the long validation period—measuring the true skill of the pseudo-reconstruction—correlations are always significant and remain close to the range of the calibration scores. Additionally, we compute two pseudo-reconstructions: $\text{NAO}_{\text{Trouet}}$ (using Morocco and Scotland pseudo-proxies) and $\text{NAO}_{\text{Lehner}}$ (an improved version of $\text{NAO}_{\text{Trouet}}$, including hypothetical proxies from the Iberian Peninsula and Scandinavia, tested in a previous perfect-model study²⁰). The performance of these pseudo-reconstructions (in terms of correlation with the simulated NAO) is evaluated in a 50-year moving window throughout the entire millennial runs, and compared with the performance of the mean NAO_{mc} ensemble (Extended Data Fig. 2). Our method (represented by the mean NAO_{mc} ensemble) shows clearly higher correlations with the simulated NAO ($r_{\text{median}} = 0.44$) than does $\text{NAO}_{\text{Trouet}}$ ($r_{\text{median}} = 0.21$), but lower values than $\text{NAO}_{\text{Lehner}}$ ($r_{\text{median}} = 0.55$). There is therefore scope for improving our model, provided that new proxy records become available at key locations, associated with strong NAO fingerprints that are unrepresented in our data set.

Finally, we address the impact of external forcings on the yearly NAO_{mc} ensemble mean. We do not detect any significant relationship with two different total solar irradiance reconstructions^{26,27}, even at the 11-year timescale (data not shown). In contrast, a composite analysis of the NAO response to the strongest 11 volcanic eruptions during the past millennium shows a significant ($P < 0.05$) positive phase appearing two years after the selected events (Fig. 4a). This result is robust, regardless of the volcanic reconstruction considered^{28–30} (Extended Data Table 6). One of the volcanic time series shows a second peak four years after the eruption, probably arising from misrepresentations in the timing of some events. By refining our selection (Fig. 4b)—now including 11 volcanoes represented in the three data sets, with eruption years cross-checked and corrected with historical records and information from local deposits (Extended Data Table 7)—we obtain a clearer response, only significant two years after the eruption when it

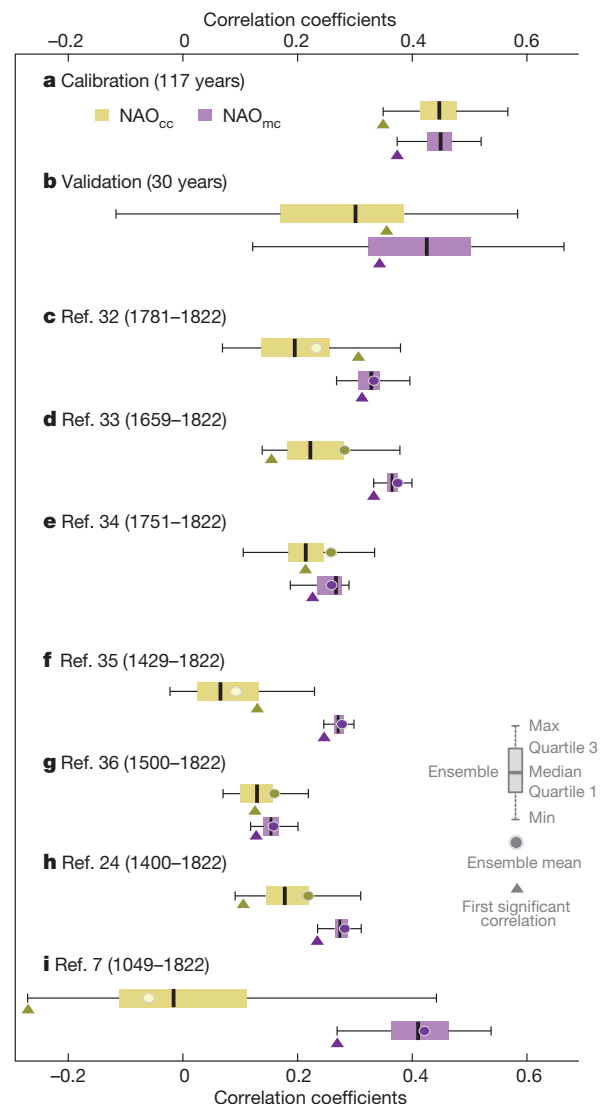


Figure 3 | Validation of the ensemble NAO reconstructions. **a, b**, Box-and-whisker plots of the correlations between the NAO_{cc} (yellow boxes), or NAO_{mc} (purple boxes), reconstruction ensembles and the instrumental $\text{NAO}_{\text{Vintner}}$ index, in the calibration (a) and validation (b) subsets, respectively. Small triangles indicate the value of the first significant correlation coefficient ($P < 0.05$) in each ensemble. **c–i**, Correlations of the same ensemble reconstructions with other reconstructed NAO time series (Extended Data Table 4). **c–e**, NAO time series from extended sea-level-pressure data sets^{32–34}, following the definition in ref. 23. **f–i**, NAO time series from other reconstructions^{7,24,35,36}. Dots represent the respective correlations with the ensemble mean; these dots are filled (or unfilled) if the correlations are significant (or insignificant).

surpasses the 95% confidence level (Fig. 4a). This positive NAO response can partly explain the predominance of positive NAO phases between AD 1150 and AD 1400, a period of increased volcanic activity. However, this response to volcanoes might be overestimated in our reconstruction owing to its strong dependence on temperature-sensitive proxies from Greenland (Fig. 1c), which can respond directly to the reduced radiative conditions. Yet the fact that, in the ice cores, the relation between the registered $\delta^{18}\text{O}$ and temperature is modulated by precipitation intermittency¹⁰, along with the lack of NAO response for the first year after the eruptions, suggests that at least part of the estimated impact of volcanoes is dynamically driven.

The identification of this volcanic influence is also consistent with observational and modelling studies^{8,9,31}, and can be considered to be an additional validation of our reconstruction at the interannual timescale. Adding this finding to the verification via pseudo-proxies and

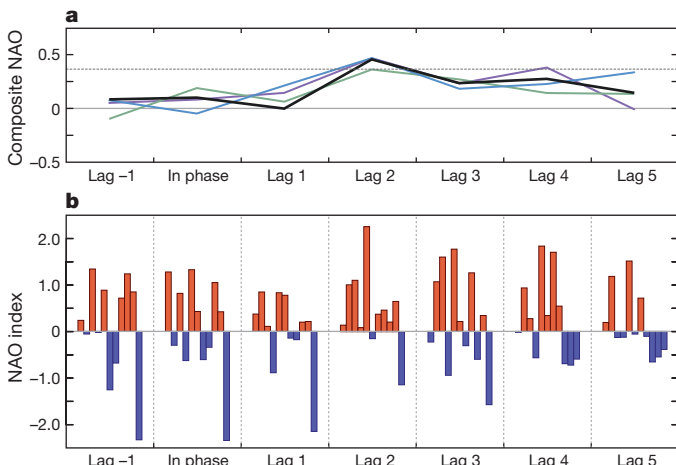


Figure 4 | NAO response to large volcanic eruptions. **a**, Composite NAO_{mc} response to the 11 strongest eruptions in three volcanic forcing reconstructions (purple line, ref. 29; blue line, ref. 28; green line, ref. 30; Extended Data Table 6), and to a refined selection of 11 intense volcanoes common to the three data sets (black line) (see Methods). Significance is assessed following a Monte Carlo approach with 1,000 random selections of 11 years from the NAO_{mc} mean reconstruction. The horizontal lines delimit the thresholds of significance at 95%. The ‘lag’ refers to the number of years after the volcanic eruption. **b**, NAO values preceding and following the onset of the 11 intense eruptions common to the three reconstructions (Extended Data Table 7).

earlier reconstructions, we conclude that the NAO_{mc} ensemble presents a robust, highly resolved estimate of NAO variability in the last millennium, providing new insights into Northern Hemisphere climatic and environmental changes during this period, and ruling out the persistence of positive phases during the MCA. Proxy records are commonly used as a benchmark with which to assess the ability of climate models to reproduce past variability. Here, we have used reanalyses and state-of-the-art climate simulations to improve the reliability of proxy reconstructions. We have demonstrated the added value of constraining the selection of proxies with reanalysis and model outputs, and encourage the use of this approach in future reconstructions.

Online Content Methods, along with any additional Extended Data display items and Source Data, are available in the online version of the paper; references unique to these sections appear only in the online paper.

Received 29 August 2014; accepted 29 April 2015.

- Hurrell, J. W. Decadal trends in the North Atlantic Oscillation: regional temperatures and precipitation. *Science* **269**, 676–679 (1995).
- Pinto, J. G., Karrenmann, M. K., Born, K., Della-Marta, P. M. & Klapwijk, M. Loss potentials associated with European windstorms under future climate conditions. *Clim. Res.* **54**, 1–20 (2012).
- Pozo-Vazquez, D., Santos-Alamillos, F., Lara-Fanego, V., Ruiz-Arias, J., Tovar-Pescador, J. & n. in *Hydrological, Socioeconomic and Ecological Impacts of the North Atlantic Oscillation in the Mediterranean Region Vol. 46 Advances in Global Change Research* (eds Vicente-Serrano, S. M. & Trigo, R. M.) Ch. 15 (Springer, 2011).
- Kettlewell, P. S., Sothern, R. B. & Koukkari, W. L. UK wheat quality and economic value are dependent on the North Atlantic Oscillation. *J. Cereal Sci.* **29**, 205–209 (1999).
- López-Moreno, J. I., Beguería, S., Vicente-Serrano, S. M. & García-Ruiz, J. M. Influence of the North Atlantic Oscillation on water resources in central Iberia: Precipitation, streamflow anomalies, and reservoir management strategies. *Wat. Resour. Res.* **43**, W09411 (2007).
- Scaife, A. A. et al. Skilful long range prediction of European and North American winters. *Geophys. Res. Lett.* **41**, 2514–2519 (2014).
- Trouet, V. et al. Persistent positive North Atlantic Oscillation mode dominated the medieval climate anomaly. *Science* **324**, 78–80 (2009).
- Graf, H. F., Kirchner, I., Robock, A. & Schulz, I. Pinatubo eruption winter climate effects: model versus observations. *Clim. Dyn.* **9**, 81–93 (1993).
- Stenchikov, G. et al. Arctic Oscillation response to the 1991 Mount Pinatubo eruption: effects of volcanic aerosols and ozone depletion. *J. Geophys. Res. D* **107**, 4803 (2002).
- Casado, M. et al. Impact of precipitation intermittency on NAO-temperature signals in proxy records. *Clim. Past* **9**, 871–886 (2013).

- Schurer, A. P., Tett, S. F. B. & Hegerl, G. C. Small influence of solar variability on climate over the past millennium. *Nature Geosci.* **7**, 104–108 (2014).
- Lamb, H. H. The early medieval warm epoch and its sequel. *Palaeogeogr. Palaeoclimatol. Palaeoecol.* **1**, 13–37 (1965).
- Olsen, J., Anderson, N. J. & Knudsen, M. F. Variability of the North Atlantic Oscillation over the past 5,200 years. *Nature Geosci.* **5**, 808–812 (2012).
- Moreno, A. et al. The Medieval Climate Anomaly in the Iberian Peninsula reconstructed from marine and lake records. *Quat. Sci. Rev.* **43**, 16–32 (2012).
- Gómez-Navarro, J. J. & Zorita, E. Atmospheric annular modes in simulations over the past millennium: no long-term response to external forcing. *Geophys. Res. Lett.* **40**, 3232–3236 (2013).
- Box, J. E. Survey of Greenland instrumental temperature records: 1873–2001. *Int. J. Climatol.* **22**, 1829–1847 (2002).
- Jones, P. D., Harpham, C. & Vinther, B. M. Winter-responding proxy temperature reconstructions and the North Atlantic Oscillation. *J. Geophys. Res. D* **119**, 6497–6505 (2014).
- Schmutz, C., Luterbacher, J., Gyalistras, D., Xoplaki, E. & Wanner, H. Can we trust proxy-based NAO index reconstructions? *Geophys. Res. Lett.* **27**, 1135–1138 (2000).
- Raible, C. C., Lehner, F., González-Rouco, J. F. & Fernández-Donado, L. Changing correlation structures of the Northern Hemisphere atmospheric circulation from 1000 to 2100 AD. *Clim. Past* **10**, 537–550 (2014).
- Lehner, F., Raible, C. C. & Stocker, T. F. Testing the robustness of a precipitation proxy-based North Atlantic Oscillation reconstruction. *Quat. Sci. Rev.* **45**, 85–94 (2012).
- Huth, R., Bochnicek, J. & Hejda, P. The 11-year solar cycle affects the intensity and annularity of the Arctic Oscillation. *J. Atmos. Sol. Terr. Phys.* **69**, 1095–1109 (2007).
- Chen, W. & Zhou, Q. Modulation of the Arctic Oscillation and the East Asian winter climate relationships by the 11-year solar cycle. *Adv. Atmos. Sci.* **29**, 217–226 (2012).
- Vinther, B. M., Andersen, K. K., Hansen, A. W., Schmitt, T. & Jones, P. D. Improving the Gibraltar/Reykjavík NAO index. *Geophys. Res. Lett.* **30**, 2222 (2003).
- Cook, E. R., D'Arrigo, R. D. & Mann, M. E. A well-verified, multiproxy reconstruction of the winter North Atlantic Oscillation index since AD 1400. *J. Clim.* **15**, 1754–1764 (2002).
- Smerdon, J. E. Climate models as a test bed for climate reconstruction methods: pseudoproxy experiments. *WIREs. Clim. Change* **3**, 63–77 (2012).
- Crowley, T. J. Causes of climate change over the past 1000 years. *Science* **289**, 270–277 (2000).
- Vieira, L. E. A., Solanki, S. K., Krivova, N. A. & Usoskin, I. Evolution of the solar irradiance during the Holocene. *Astron. Astrophys.* **531**, A6 (2011).
- Crowley, T. J. & Unterman, M. B. Technical details concerning development of a 1200 yr proxy index for global volcanism. *Earth Syst. Sci. Data* **5**, 187–197 (2013).
- Gao, C., Robock, A. & Ammann, C. Volcanic forcing of climate over the past 1500 years: an improved ice core-based index for climate models. *J. Geophys. Res.* **113**, D23111 (2008).
- Sigl, M. et al. Insights from Antarctica on volcanic forcing during the Common Era. *Nature Clim. Change* **4**, 693–697 (2014).
- Shindell, D. T., Schmidt, G. A., Mann, M. E. & Faluvegi, G. Dynamic winter climate response to large tropical volcanic eruptions since 1600. *J. Geophys. Res. D* **109**, D05104 (2004).
- Jones, P. D. et al. Monthly mean pressure reconstructions for Europe. *Int. J. Climatol.* **19**, 347–364 (1999).
- Luterbacher, J. et al. Reconstruction of sea level pressure fields over the Eastern North Atlantic and Europe back to 1500. *Clim. Dyn.* **18**, 545–561 (2002).
- Küttel, M. et al. The importance of ship log data: reconstructing North Atlantic, European and Mediterranean sea level pressure fields back to 1750. *Clim. Dyn.* **34**, 1115–1128 (2010).
- Glueck, M. F. & Stockton, C. W. Reconstruction of the North Atlantic Oscillation, 1429–1983. *Int. J. Climatol.* **21**, 1453–1465 (2001).
- Luterbacher, J. et al. Extending North Atlantic oscillation reconstructions back to 1500. *Atmos. Sci. Lett.* **2**, 114–124 (2001).

Supplementary Information is available in the online version of the paper.

Acknowledgements The work of P.O., D.S., V.M.-D. and M.C. has been financially supported by the French ANR CEPS project Green Greenland (ANR-10-CEPL-0008). F.L. and C.R. acknowledge the support of the NCCR-Climate, funded by the Swiss National Science Foundation (grant number 200020 147174). P.Y. acknowledges funding from the Swedish Research Council (grant number C0629701). We thank the paleoclimate community, in particular the PAGES2k Network, and all the institutions involved in the CMIP5/PMIP3 initiative for making available proxy data and model outputs. We also thank F. González-Rouco and M. Montoya for discussions at an earlier stage of the analysis; M. Khodri for feedback on the volcanic reconstructions; and E. Hawkins for help and advice on the statistical analysis.

Author Contributions P.O. gathered and prepared the data with the help of M.C., and developed the ensemble reconstruction and part of the statistical analyses. F.L. prepared the pseudo-proxies from reanalyses and models and carried out the perfect-model study. D.S. analysed the impact of external forcings on the NAO. All authors helped in conceiving the study, discussing ideas and writing the paper.

Author Information Data will be made available at <http://www.ncdc.noaa.gov/data-access/paleoclimatology-data>. Reprints and permissions information is available at www.nature.com/reprints. The authors declare no competing financial interests. Readers are welcome to comment on the online version of the paper. Correspondence and requests for materials should be addressed to P.O. (pablo.ortega@lsce.ipsl.fr).

METHODS

Analysis of significance. In the initial proxy selection of Fig. 1a, proxies are required to significantly correlate with $\text{NAO}_{\text{Vinther}}$ at the 90% confidence level. This threshold is not particularly restrictive and allows the identification of a large number of candidate time series that are potentially linked to the NAO. Since the final selection of proxies is later constrained during the calibration process, and also with reanalysis and model outputs, the risk of including time series with a spurious relationship with the NAO is small. All subsequent correlations are assessed by correcting the sample size to take into account the autocorrelation. The confidence level is kept at 90% when proxies are evaluated and in the different PCR steps, and increased to 95% for the estimation of the validation/calibration scores, and when comparing the reconstruction against other data sets. For the composite analysis of volcanic events (Fig. 4), significance is assessed at the 95% confidence level, following a Monte Carlo approach with 1,000 random equivalent selections. A confidence level of 95% is also applied for a two-tailed Student's *t*-test in assessing when a 100-year running average of the NAO ensemble mean is different from zero (horizontal bars in Fig. 2).

Selection of proxies. The initial set of proxy records (Extended Data Table 1) is the result of an extensive search throughout different palaeoclimate data repositories, such as the International Tree-Ring Data Bank (ITRDB; <https://www.ncdc.noaa.gov/data-access/paleoclimatology-data/datasets/tree-ring>), <http://www.ncdc.noaa.gov/data-access/paleoclimatology-data>, and <http://www.pangaea.de/>. Many proxies (>150) from the Northern Hemisphere were found to meet the two imposed criteria: annual resolution and continuous time coverage from the eleventh to the twentieth century. These proxies were further screened for their correlation with $\text{NAO}_{\text{Vinther}}$ at the 90% confidence level. Only the 48 proxies used in our analysis met this condition.

Climatic interpretation of proxies. Both the seasonality and the climate variable associated with each proxy were extracted either from the original references detailed in Extended Data Table 1, or from subsequent references making use of them. For instance, a few tree-ring proxy records (such as Lily Lake) are interpreted herein in terms of annual temperature as they have already contributed to several multi-proxy reconstructions for past global and continental temperature^{37,38}. When two possible climatic interpretations of the same proxy record exist, we kept the one leading to the highest correlations with the NAO in the twentieth century reanalysis (for example, Mammoth Peak as winter precipitation instead of summer temperature).

Potential biases in the representation of low-frequency variability. No post-processing has been applied to any of the proxy time series considered. All chronologies therefore correspond to the source data as they were originally provided. Note that the tree-ring records might lack some part of their low-frequency variability owing to the age-trend removal techniques. The degree of variance sacrificed may vary substantially from one record to another, because some research groups privilege more conservative detrending methods, and others prefer to retain as much low-frequency variability as possible. Ice-core records are also generally corrected for postdepositional effects, such as firn diffusion, or ice flow in the Greenland ice sheet. Firn diffusion affects only subannual variability, and may introduce biases in the seasonally resolved records. It does not affect low-frequency variability or trends. Ice flow is important only in regions of significant ice-flow rate, such as the DYE-3 drill site, and requires flow models to be corrected; it might affect to some degree the realism of the long-term trends. Other potential low-frequency biases relate to bandwidth speleothem measurements and varved lake sediments that need to be corrected for nonhomogenous growth rates and compactness, respectively. More generally, all proxy records are affected to some extent by local environmental changes (such as wind scouring for ice cores), which can perturb the recorded climatic signal. This is why it is important to perform multi-proxy reconstructions—so that most of these potential biases can be cancelled out, and the common climate signal better identified.

PCR calculation. The reconstruction method is based on a previous study²³ that uses a nested PCR to gradually adjust to the changing number of source proxy records available in consecutive periods of 25 years. Here, we consider only proxies that extend with no interruption from the eleventh to the twentieth century, so only one PCR needs to be calculated (for each ensemble realization). The PCR approach is applied as follows: all selected proxy records are first standardized with respect to the common period AD 1823–1969, and used to define a matrix (in time and space) for the period common to all proxies. This period can change depending on the actual selection, the shortest being from AD 1073 to AD 1969 when the proxy record from Firth River is available. For each ensemble realization, the corresponding subset of years previously set for calibration is extracted from that matrix. A principal-components analysis (PCA) of this reduced matrix is performed afterwards. Preisendorfer's rule-N³⁹ is then applied to discard those principal components (PCs) whose explained variability is undistinguishable (at the 95% significance level) from that of a matrix of red-noise processes composed of

the first autoregressive models, AR(1), of the original proxies. For this assessment, 300 independent gaussian white-noise matrices are generated (with the same dimensions as the reduced one), and a PCA is applied to each of them. In each realization, the PCs are organized in decreasing order of their variance across the Gaussian set. We then take all of the first PCs, and establish the 95th percentile of the associated variances. This step is repeated from the second to the last PC. The 95th-percentile values thus obtained are used as significance thresholds for the truncation of the original PCs. The aim of this truncation is to retain all the modes with relevant climate information, and to use them to produce a multivariate linear regression model of the NAO. To extend the reconstruction back to the eleventh century, the complete matrix of predictors is projected into the eigenvectors of the selected PCs (also known as empirical orthogonal functions, EOFs), fitting by least squares. These projections describe the variability associated with each EOF over the whole time extent of the matrix of predictors, and coincide with the original PCs in the calibration period. These are the series feeding the multivariate model to produce the actual NAO reconstruction. To correct for the loss in variance inherent to the multiple regression, the final NAO time series is restandardized with respect to the calibration period. No trends are removed before the PCR analysis, since they are also essential to reproduce the past NAO variability. This is a standard reconstruction practice^{24,32}.

Proxy contribution to the ensemble reconstruction. In each individual PCR reconstruction, the beta-weights of the proxies are obtained as in ref. 24: we multiply the vector of the standardized regression coefficients (also known as beta-weights on the PC space) by the matrix of the retained eigenvectors. In practice, for an individual proxy record *i*, this corresponds to:

$$\beta(i) = \sum_{j=1}^n c_j \cdot \omega_j(i)$$

where $\beta(i)$ denotes the beta-weight of the given proxy, n the number of predictors (that is, PCs) participating in the multivariate regression, c_j the regression coefficient for the predictor *j*, and ω_j the loading associated with the proxy *i* in the eigenvector of predictor *j*. The beta-weight of the proxy *i* in the ensemble mean reconstruction is obtained as the sum of its respective beta-weights in the individual realizations.

Estimation of reconstruction uncertainties. Our method accounts only for regression-based uncertainties associated with the residuals in the calibration period. These are represented by the s.e. of the regression, calculated as the square root of the sum of the squared residuals divided by the degrees of freedom:

$$\text{s.e.} = \sqrt{\frac{\sum_{t=1}^n \varepsilon_t^2}{(n-2)}} = \sqrt{\frac{\sum_{i=1}^n (y_i - \hat{y}_i)^2}{(n-2)}}$$

where n represents the number of time steps in the calibration period, ε the residuals, y the predicted, and \hat{y} the reconstructed variable.

Standard errors are calculated for each of the 100 selected individual reconstructions. In each of them, the uncertainty band is set at ± 2 s.e. The envelope of these bands across the different ensemble members is included in Fig. 2 to describe the total uncertainty range of each ensemble reconstruction. The perfect-model analysis supports the validity of this approach, with only about 2% of years falling outside the ± 2 s.e. envelope. The characterization of other sources of uncertainty (such as chronological errors) lies beyond the scope of our analysis.

Sensitivity to the reconstruction choices. Several alternative ensemble reconstructions have been performed to test the sensitivity to some of the choices in our approach. Overall, the reconstructions and the main findings remain coherent. For instance, increasing the validation period to 40 years (and reducing the calibration subsequently to 107) barely affects the final NAO_{mc} ensemble mean reconstruction. Similar results also hold if Preisendorfer's rule-N is based on a white noise floor assumption, or if proxy selection is constrained only through reanalyses or PMIP3 simulations. Additional criteria for ensemble generation, such as subsampling the proxies depending on their kind, are found to increase the uncertainty bars because of the poor skill of some members, but have a minor effect on the variability described by the mean ensemble reconstruction.

Model-constrained ensemble reconstructions. Given some known deficiencies in the reanalyses in terms of accurately representing variables such as precipitation in high-elevation regions (for example, Greenland or the Alps), and considering that reanalyses have different spatial resolutions and cover different time periods (Extended Data Table 2) with different degrees of confidence, we apply a relaxed constraint, so that any proxy with a significant relationship with the NAO in any of the four reanalyses is kept. Similarly, since not all PMIP3 models are equally realistic in the representation of the NAO fingerprints on surface climate⁴⁰, but keeping in mind that with them we test the robustness and stability of the teleconnections, the ensemble NAO_{mc} reconstruction is additionally constrained to

those proxy records that correlate significantly with the NAO in at least half of the eight PMIP3 simulations.

Perfect-model approach. This technique is used to test the adequacy or realism of different assumptions or methods. It is based on the use of model outputs as substitute climate records that can be used, for instance, to assess the performance of different reconstruction strategies^{41,42}, or the potential of decadal predictions (both statistical⁴³ and dynamical^{44,45}). The model is assumed to be ‘perfect’ in the sense that it describes an idealized surrogate reality, where climate variations are physically consistent, without any measurement uncertainty, and are accessible everywhere without restrictions and for the whole extent of the simulations. In our analysis, we mimic the original proxies with model outputs (see below), and use these pseudo-proxies to reproduce the different steps of our reconstruction approach, but within the model world. One of the main advantages that this perfect model framework offers is that validation scores can also be estimated outside of the observational period AD 1823–1969. This is particularly interesting, since it allows a validation over a long time frame (AD 1000–1822), and thus provides a test of the stability of the assumed teleconnections.

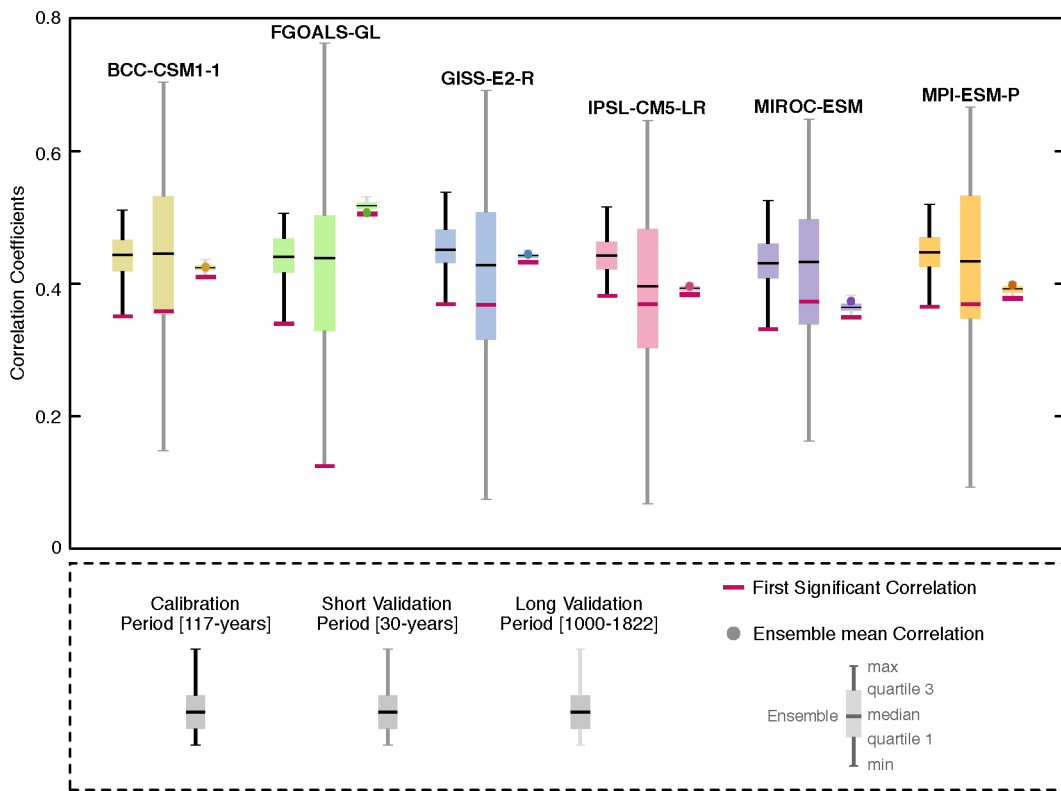
Pseudo-proxy definition. All pseudo-proxies are defined as a 2×2 average of the related climate variable centred on the proxy location, using the same reported seasonal window (Extended Data Table 1). These are the series used to identify the proxies that are consistent with the reanalyses and the PMIP3 simulations (Fig. 1c). The pure simulated climatic signal is later perturbed with noise for the perfect-model analysis. The noise is estimated as an AR(1) process that describes the residual of subtracting the normalized real proxy from normalized observational data at the same location. Temperature data are retrieved from Berkeley Earth (<http://berkeleyearth.org/data>) and precipitation from the Climate Research Unit (<http://badc.nerc.ac.uk/browse/badc/cru>) data sets. Our approach therefore mimics the actual noise that arises from relating a proxy signal to a single climate variable. Ten alternative pseudo-proxies are generated for ten different realizations of the noise (Extended Data Fig. 3). For the perfect-model analysis, we use the pseudo-proxy whose correlation with the simulated NAO is closer to that of the actual proxy with $\text{NAO}_{\text{Vinther}}$. This is done to be more representative of the real proxy sensitivity. The hypothetical pseudo-proxies from Spain and Norway (where no real proxy is yet available), which are necessary for the $\text{NAO}_{\text{Lehner}}$ pseudo-reconstruction, were generated by adding Gaussian noise with properties similar to those of the twentieth century reanalysis at these locations.

Identification of strong volcanic eruptions. This analysis uses the three latest published reconstructions of past volcanic activity covering the past millennium. Two of them^{28,29} combine volcanic-related information from Greenland and Antarctic ice cores, although they differ in the source records and the calibration strategy. The third reconstruction³⁰ is based exclusively on an extensive array of Antarctic ice cores, most of them not included in the former reconstructions. The combination of multiple ice-core records is an important step, accounting for age-scale and deposition uncertainties. The three reconstructions show important discrepancies regarding the timing and relative magnitude of some eruptions. This is illustrated through the selection of the 11 strongest events in each volcanic reconstruction (Extended Data Table 6). We first identify the strongest volcano according to the related reconstructed variable, and screen out all dates that are 3 years before or after the eruption (to avoid double selections). This process is repeated with the remaining dates until 11 events have been identified. Note that even when a specific eruption is present in the three volcanic series, the uncertainty in the year of occurrence can be as large as 2 years (for example, 1284, 1286, 1285). To reduce this timing uncertainty, and to ensure that we select only well supported volcanic eruptions, we extract the 25 largest eruptions in each volcanic chronology (not shown), and compare them to identify the episodes common to all reconstructions (within a ± 3 year range). This leads to a final selection of 11 common volcanoes (Extended Data Table 7). The final adopted dates for the composite analysis in Fig. 4 are extracted from historical sources (<http://www.volcano.si.edu/>)⁴⁶ or other reliable sedimentary records⁴⁷. For the three unknown eruptions, for which no additional information is available, we took either the most repeated date, or the average date of the three reconstructions.

Code availability. The code used to produce the model-constrained ensemble reconstruction is available in the Supplementary Information.

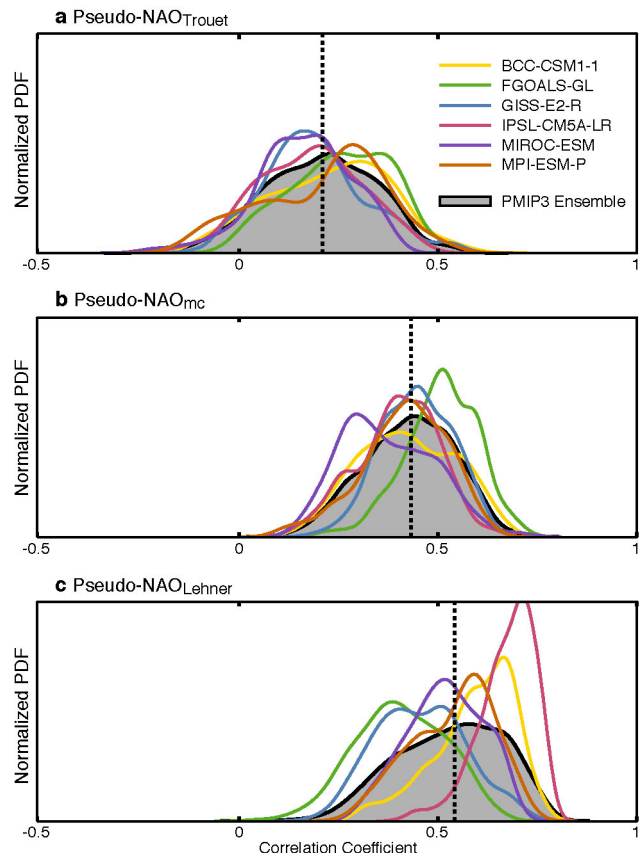
37. Mann, M. E. *et al.* Proxy-based reconstructions of hemispheric and global surface temperature variations over the past two millennia. *Proc. Natl Acad. Sci. USA* **105**, 13252–13257 (2008).
38. Ahmed, M. *et al.* Continental-scale temperature variability during the past two millennia. *Nature Geosci.* **6**, 339–346 (2013).
39. Overland, J. E. & Preisendorfer, R. W. A significance test for principal components applied to a cyclone climatology. *Mon. Weath. Rev.* **110**, 1–4 (1982).
40. Davini, P. & Cagnazzo, C. On the misinterpretation of the North Atlantic Oscillation in CMIP5 models. *Clim. Dyn.* **43**, 1497–1511 (2014).
41. Baehr, J., Hirschi, J., Beismann, J. O. & Marotzke, J. Monitoring the meridional overturning circulation in the North Atlantic: a model-based array design study. *J. Mar. Res.* **62**, 283–312 (2004).
42. González-Rouco, J., Beltrami, H., Zorita, E. & von Storch, H. Simulation and inversion of borehole temperature profiles in surrogate climates: spatial distribution and surface coupling. *Geophys. Res. Lett.* **33**, L01703 (2006).
43. Hawkins, E., Robson, J., Sutton, R., Smith, D. & Keenlyside, N. Evaluating the potential for statistical decadal predictions of sea surface temperatures with a perfect model approach. *Clim. Dyn.* **37**, 2495–2509 (2011).
44. Griffies, S. M. & Bryan, K. A predictability study of simulated North Atlantic multidecadal variability. *Clim. Dyn.* **13**, 459–487 (1997).
45. Collins, M. & Sinha, B. Predictability of decadal variations in the thermohaline circulation and climate. *Geophys. Res. Lett.* **30**, 1306 (2003).
46. Siebert, L., Simkin, T. & Kimberly, P. *Volcanoes of the World* 3rd edn (Univ. California Press, 2010).
47. Lavigne, F. *et al.* Source of the great A.D. 1257 mystery eruption unveiled, Samalas volcano, Rinjani volcanic complex, Indonesia. *Proc. Natl Acad. Sci. USA* **110**, 16742–16747 (2013).
48. Miller, H. & Schwager, M. Accumulation rate and stable oxygen isotope ratios of ice core ngt14C93.2 from the North Greenland Traverse. <http://dx.doi.org/10.1594/PANGAEA.57158> (2000).
49. Andersen, K. K. *et al.* Retrieving a common accumulation record from Greenland ice cores for the past 1800 years. *J. Geophys. Res.* **111**, D15106 (2006).
50. Cuffey, K. M. *et al.* Large Arctic temperature change at the Wisconsin-Holocene glacial transition. *Science* **270**, 455–458 (1995).
51. Fisher, D. A., Koerner, R. M. & Reeh, N. Holocene climatic records from Agassiz Ice Cap, Ellesmere Island, NWT, Canada. *Holocene* **5**, 19–24 (1995).
52. Vinther, B. M. *et al.* Climatic signals in multiple highly resolved stable isotope records from Greenland. *Quat. Sci. Rev.* **29**, 522–538 (2010).
53. Grootes, P. & Stuiver, M. Oxygen 18/16 variability in Greenland snow and ice with 10^{-3} to 10^3 year time resolution. *J. Geophys. Res.* **102**, 26455–26470 (1997).
54. Wilhelm, B. *et al.* 1400 years of extreme precipitation patterns over the Mediterranean French Alps and possible forcing mechanisms. *Quat. Res.* **78**, 1–12 (2012).
55. Moore, J. J., Hughen, K. A., Miller, G. H. & Overpeck, J. T. Little Ice Age recorded in summer temperature reconstruction from varved sediments of Donard Lake, Baffin Island, Canada. *J. Paleolimnol.* **25**, 503–517 (2001).
56. Larsen, D. J., Miller, G. H., Geirsdóttir, A. & Thorarson, T. A 3000-year varved record of glacier activity and climate change from the proglacial lake Hvítárvatn, Iceland. *Quat. Sci. Rev.* **30**, 2715–2731 (2011).
57. Cook, T. L., Bradley, R. S., Stoner, J. S. & Francus, P. Five thousand years of sediment transfer in a high arctic watershed recorded in annually laminated sediments from Lower Murray Lake, Ellesmere Island, Nunavut, Canada. *J. Paleolimnol.* **41**, 77–94 (2009).
58. McCabe-Glynn, S. *et al.* Variable North Pacific influence on drought in southwestern North America since AD 854. *Nature Geosci.* **6**, 617–621 (2013).
59. Proctor, C., Baker, A., Barnes, W. & Gilmour, M. A thousand year speleothem proxy record of North Atlantic climate from Scotland. *Clim. Dyn.* **16**, 815–820 (2000).
60. Seim, A. *et al.* Climate sensitivity of a millennium-long pine chronology from Albania. *Clim. Res.* **51**, 217–228 (2012).
61. Büntgen, U., Frank, D. C., Nievergelt, D. & Esper, J. Summer temperature variations in the European Alps. *A.D. 755–2004*. *J. Clim.* **19**, 5606–5623 (2006).
62. Stahle, D. W. *International Tree-Ring Data Bank AR050*. <https://www.ncdc.noaa.gov/data-access/paleoclimatology-data/datasets/tree-ring> (1996).
63. Stahle, D. W. & Cleaveland, M. K. *International Tree-Ring Data Bank FL001*. <https://www.ncdc.noaa.gov/data-access/paleoclimatology-data/datasets/tree-ring> (2005).
64. Briffa, K. R. *et al.* Trends in recent temperature and radial growth spanning 2000 years across northwest Eurasia. *Phil. Trans. R. Soc.* **363**, 2271–2284 (2008).
65. Tosh, R. *International Tree-Ring Data Bank CA051*. <https://www.ncdc.noaa.gov/data-access/paleoclimatology-data/datasets/tree-ring> (1994).
66. Bunn, A. G., Graumlich, L. J. & Urban, D. L. Trends in twentieth-century tree growth at high elevations in the Sierra Nevada and White Mountains, USA. *Holocene* **15**, 481–488 (2005).
67. Woodhouse, C. A. & Brown, P. M. *International Tree-Ring Data Bank CO572*. <https://www.ncdc.noaa.gov/data-access/paleoclimatology-data/datasets/tree-ring> (2006).
68. Anchukaitis, K. J. *et al.* Tree-ring-reconstructed summer temperatures from northwestern North America during the last nine centuries. *J. Clim.* **26**, 3001–3012 (2013).
69. Young, G. H. F. *et al.* Changes in atmospheric circulation and the Arctic Oscillation preserved within a millennial length reconstruction of summer cloud cover from northern Fennoscandia. *Clim. Dyn.* **39**, 495–507 (2012).
70. Büntgen, U., Frank, D., Neunschwendter, T. & Esper, J. Fading temperature sensitivity of Alpine tree growth at its Mediterranean margin and associated effects on large-scale climate reconstructions. *Clim. Change* **114**, 651–666 (2012).
71. Stahle, D. W. *International Tree-Ring Data Bank LA001*. <https://www.ncdc.noaa.gov/data-access/paleoclimatology-data/datasets/tree-ring> (1996).
72. Esper, J. *et al.* Long-term drought severity variations in Morocco. *Geophys. Res. Lett.* **34**, L17702 (2007).
73. Graumlich, L. J., Pisaric, M. F. J., Waggoner, L. A., Littell, J. S. & King, J. C. Upper Yellowstone River flow and teleconnections with Pacific basin climate variability during the past three centuries. *Clim. Change* **59**, 245–262 (2003).
74. Touchan, R., Woodhouse, C. A., Meko, D. M. & Allen, C. Millennial precipitation reconstruction for the Jemez Mountains, New Mexico, reveals changing drought signal. *Int. J. Climatol.* **31**, 896–906 (2011).

75. Esper, J. *et al.* Orbital forcing of tree-ring data. *Nature Clim. Change* **2**, 862–866 (2012).
76. Graybill, D. A. *International Tree-Ring Data Bank NV516*. <https://www.ncdc.noaa.gov/data-access/paleoclimatology-data/datasets/tree-ring> (1994).
77. Graybill, D. A. *International Tree-Ring Data Bank NV517*. <https://www.ncdc.noaa.gov/data-access/paleoclimatology-data/datasets/tree-ring> (1994).
78. Salzer, M. & Kipfmüller, K. Reconstructed temperature and precipitation on a millennial timescale from tree-rings in the Southern Colorado Plateau, USA. *Clim. Change* **70**, 465–487 (2005).
79. Stahle, D. W. & Cleaveland, M. K. Tree-ring reconstructed rainfall over the southeastern USA during the medieval warm period and the little ice age. *Clim. Change* **26**, 199–212 (1994).
80. Naurzbaev, M. M., Vaganov, E. A., Sidorova, O. V. & Schweingruber, F. H. Summer temperatures in eastern Taimyr inferred from a 2427-year late-Holocene tree-ring chronology and earlier floating series. *Holocene* **12**, 727–736 (2002).
81. Buntgen, U. *et al.* Filling the Eastern European gap in millennium-long temperature reconstructions. *Proc. Natl Acad. Sci. USA* **110**, 1773–1778 (2013).
82. Schweingruber, F. H. *International Tree-Ring Data Bank SWIT177*. <https://www.ncdc.noaa.gov/data-access/paleoclimatology-data/datasets/tree-ring..>
83. Graybill, D. A. *International Tree-Ring Data Bank UT508*. <https://www.ncdc.noaa.gov/data-access/paleoclimatology-data/datasets/tree-ring> (1994).
84. Graybill, D. A. *International Tree-Ring Data Bank UT509*. <https://www.ncdc.noaa.gov/data-access/paleoclimatology-data/datasets/tree-ring> (1994).
85. Kalnay, E. *et al.* The NCEP/NCAR 40-year reanalysis project. *Bull. Am. Meteorol. Soc.* **77**, 437–471 (1996).
86. Compo, G. *et al.* The twentieth century reanalysis project. *Q. J. R. Meteorol. Soc.* **137**, 1–28 (2011).
87. Dee, D. P. *et al.* The ERA-interim reanalysis: configuration and performance of the data assimilation system. *Q. J. R. Meteorol. Soc.* **137**, 553–597 (2011).
88. Uppala, S. M. *et al.* The ERA-40 re-analysis. *Q. J. R. Meteorol. Soc.* **131**, 2961–3012 (2005).
89. Zhang, J. & Wu, T. W. The impact of external forcings on climate during the past millennium: Results from transient simulation with BCC_CSM1.1. *European Geosciences Union General Assembly abstr. EGU2012-448* (2012).
90. Landrum, L. *et al.* Last millennium climate and its variability in CCSM4. *J. Clim.* **26**, 1085–1111 (2012).
91. Phipps, S. *et al.* The CSIRO Mk3L climate system model version 1.0—Part 2: response to external forcings. *Geosci. Model Dev.* **5**, 649–682 (2012).
92. Zhou, T., Li, B., Man, W., Zhang, L. & Zhang, J. A comparison of the Medieval Warm Period, Little Ice Age and 20th century warming simulated by the FGOALS climate system model. *Chin. Sci. Bull.* **56**, 3028–3041 (2011).
93. Schmidt, G. A. *et al.* Configuration and assessment of the GISS ModelE2 contributions to the CMIP5 archive. *J. Adv. Model. Earth Syst.* **6**, 141–184 (2014).
94. Sueyoshi, T. *et al.* Set-up of the PMIP3 paleoclimate experiments conducted using an Earth system model, MIROC-ESM. *Geosci. Model Dev. Discuss.* **6**, 819–836 (2013).
95. Jungclaus, J. H., Lohmann, K. & Zanchettin, D. Enhanced 20th century heat transfer to the Arctic simulated in the context of climate variations over the last millennium. *Clim. Past* **10**, 2895–2924 (2014).

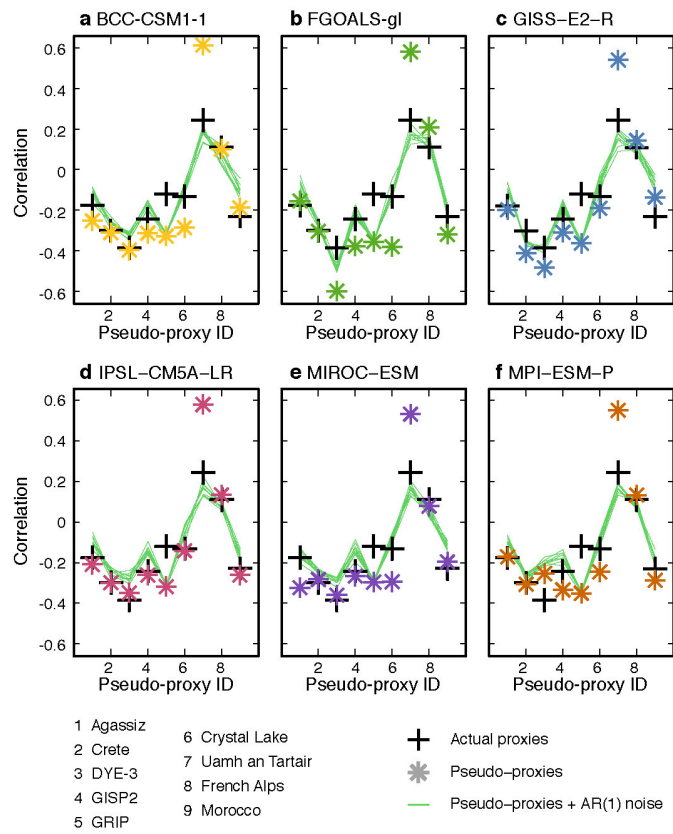


Extended Data Figure 1 | Verification of the pseudo-reconstructions. Box-and-whisker plots showing the correlations between the six pseudo-reconstructed NAO_{mc} ensembles and the corresponding true simulated NAOs, in three independent subsets of years (from left to right for each ensemble): the 117 years selected for calibration (specific to each ensemble realization), the remaining 30 years that need to be validated (following the original strategy),

and a long validation period from AD 1000–1822 (possible thanks to the perfect-model approach). In this latter case, since the period is the same for all the ensemble realizations, the correlation is also calculated for the ensemble mean (filled coloured dots). Red horizontal lines indicate the first significant correlation coefficient ($P < 0.05$) of the ensemble.



Extended Data Figure 2 | Comparison of three alternative reconstructions.
The figure shows probability density functions (PDFs) for the 50-year moving-window correlations between the simulated NAO and three alternative pseudo-reconstructions in the ensemble of PMIP3 simulations (Extended Data Table 3): **a**, NAO_{Trouet}; **b**, NAO_{mc}; **c**, NAO_{Lehner}. Vertical dotted lines represent the median correlation for the ensemble. Each coloured line represents a different pseudo-reconstructed NAO ensemble.



Extended Data Figure 3 | NAO–pseudo-proxy relationships.
a–f, Correlations between the simulated NAO and the associated pseudo-proxies in the PMIP3 runs. Pseudo-proxies are defined from a pure climatic signal (coloured asterisks), and subsequently perturbed with AR(1) noises (thin green lines). For the perturbed pseudo-proxy definitions, ten different realizations of the noise are considered. The correlations between the actual proxies and $\text{NAO}_{\text{Vinther}}$ in the common period AD 1823–1969 are also shown for comparison (thick black crosses).

Extended Data Table 1 | Proxy description

N	Site	Archive	Proxy type	LON	LAT	Time Span	Correlation in overlap period	Related variable	Seasonality	Refs
1	B18	Ice core	Snow Accumulation	-36.4	76.6	1000-1992	0.19	Precip	Annual	48
2	Crete	Ice core	Snow Accumulation	-39.7	71	1000-1973	-0.19	Precip	Annual	49
3	GISP2	Ice core	Snow Accumulation	-40.9	72.5	1000-1988	-0.12	Precip	Annual	50
4	Agassiz (A79)*	Ice core	$\delta^{18}\text{O}^\dagger$	-73.1	80.7	1000-1972	-0.18	SAT	Annual	51
5	Crete	Ice core	$\delta^{18}\text{O}^\dagger$	-37.3	71.1	1000-1973	-0.31	SAT	NDJFMA	52
6	DYE-3 (stack)	Ice core	$\delta^{18}\text{O}^\dagger$	-43.8	65.2	1000-1978	-0.39	SAT	NDJFMA	52
7	GISP2	Ice core	$\delta^{18}\text{O}^\dagger$	-38.5	72.6	1000-1987	-0.21	SAT	Annual	53
8	GRIP	Ice core	$\delta^{18}\text{O}^\dagger$	-37.5	72.6	1000-1979	-0.13	SAT	NDJFMA	52
9	Allos Lake	Lake Sediment	Flood deposit thickness	6.7	44.2	1000-2009	0.11	Precip	SON	54
10	Donard Lake	Lake Sediment	Varve thickness	-61.4	66.7	1000-1995	-0.14	SAT	JJA	55
11	Hvítárvatn Lake	Lake Sediment	Varve thickness	-19.8	64.6	1000-2000	-0.11	SAT	JJAS	56
12	Lower Murray Lake	Lake Sediment	Mass accumulation	-69.5	81.3	1000-1969	-0.18	SAT	JJA	57
13	Crystal Cave	Speleothem	$\delta^{18}\text{O}^\dagger$	-18.8	36.6	1000-2007	-0.15	SAT	Annual	58
14	Uamh an Tartair	Speleothem	Bandwidth	-4.9	58.1	1000-1995	0.24	Precip	DJFM	59
15	Balkan Peninsula	Tree ring	Tree-ring width	20.0	41.0	1000-2008	-0.10	SAT	February	60
16	European Alps	Tree ring	Tree-ring MXD	7.5	46.0	1000-2004	0.11	SAT	JJAS	61
17	Black Swamp	Tree ring	Tree-ring width	-91.3	35.2	1019-1980	0.16	SAT	Annual	62
18	Mayberry Slough	Tree ring	Tree-ring width	-91.3	35.6	1000-1990	0.12	SAT [‡]	Annual	63
19	Avam-Taimyr	Tree ring	Tree-ring width	101.0	72.0	1000-2000	-0.10	SAT	July	64
20	San Gorgonio	Tree ring	Tree-ring width	-116.8	34.1	1000-1970	0.19	SAT	Annual	65
21	Flower Lake	Tree ring	Tree-ring width	-118.4	36.8	1000-1987	-0.14	Precip	NDJFM	66
22	Timber Gap Upper	Tree ring	Tree-ring width	-118.6	36.5	1000-1987	-0.13	Precip	NDJFM	66
23	Cirque Peak	Tree ring	Tree-ring width	-118.2	36.5	1000-1987	-0.13	Precip	NDJFM	66
24	Mammoth Peak	Tree ring	Tree-ring width	-119.3	37.9	1000-1996	-0.10	Precip	NDJFM	66
25	Boreal Plateau	Tree ring	Tree-ring width	-118.6	36.5	1000-1992	-0.14	Precip	NDJFM	66
26	Upper Wright Lakes	Tree ring	Tree-ring width	-118.4	36.6	1000-1992	-0.14	Precip	NDJFM	66
27	Hamilton	Tree ring	Tree-ring width	-118.9	37.0	1000-1988	-0.22	Precip	NDJFM	66
28	Lily Lake	Tree ring	Tree-ring width	-105.6	40.3	1000-1998	-0.12	SAT [‡]	Annual	67
29	Firth River	Tree ring	Tree-ring MXD	-141.6	68.7	1073-2002	0.14	SAT	JJA	68
30	Choctawhatchee River	Tree ring	Tree-ring width	-85.9	30.5	1000-1992	0.14	SAT [‡]	Annual	63
31	Forfjordalen	Tree ring	Tree-ring $\delta^{13}\text{C}$	15.7	68.8	1000-2001	-0.14	Cloud%	JJA	69
32	French Alps	Tree ring	Tree-ring width	7.5	44.0	1000-2007	0.10	SAT	AMJJA	70
33	Big Cypress	Tree ring	Tree-ring width	-93.0	32.3	1000-1988	0.10	SAT [‡]	Annual	71
34	Morocco	Tree ring	Tree-ring width	-5.0	33.8	1049-2001	-0.24	SPI	FMAMJ	72
35	Yellow Mountain Ridge I	Tree ring	Tree-ring width	-111.3	45.3	1000-1998	-0.13	Precip	NDJFM	73
36	Yellow Mountain Ridge I (Entire Bark Trees)	Tree ring	Tree-ring width	-111.3	45.3	1000-1998	-0.11	Precip	NDJFM	73
37	Mesa Alta	Tree ring	Tree-ring width	-106.6	36.2	1000-2007	0.13	Precip	ONDJFMAMJ	74
38	Finland	Tree ring	Tree-ring MXD	25.0	68.0	1000-2006	-0.11	SAT	JJA	75
39	Hill 10842	Tree ring	Tree-ring width	-114.2	38.9	1000-1984	0.20	SAT [‡]	Annual	76
40	Springs Mountains Lower	Tree ring	Tree-ring width	-115.7	36.3	1000-1984	0.11	SAT	Annual	77
41	S. Colorado Plateau I	Tree ring	Tree-ring width	-110.0	37.0	1000-1987	0.18	Precip	October-July	78
42	S. Colorado Plateau II	Tree ring	Tree-ring width	-110.0	37.0	1000-1996	-0.11	SAT	Annual	78
43	Four Holes Swamp	Tree ring	Tree-ring width	-80.4	33.2	1001-1985	-0.10	Precip	MAMJ	79
44	Taimyr - Putoran	Tree ring	Tree-ring width	103.0	71.3	1000-1996	-0.11	SAT	Annual	80
45	Tatra Region	Tree ring	Tree-ring width	20.0	49.0	1040-2011	-0.12	SAT	May-June	81
46	Lauenen+ div. Stao	Tree ring	Tree-ring width	7.2	46.4	1000-1976	0.14	SAT	JJA	82
47	Wild Horse Ridge	Tree ring	Tree-ring width	-111.1	39.4	1000-1985	0.19	SAT [‡]	Annual	83
48	Mammoth Creek	Tree ring	Tree-ring width	-112.7	37.7	1000-1989	0.18	SAT [‡]	Annual	84

* Proxies participating in the NAO_{mc} reconstruction are highlighted in bold.[†] Isotope values are referred to Vienna Standard Mean Ocean Water (VSMOW).[‡] These proxy records are sensitive to negative changes in the related variable.

Data are from refs 48, 49, 50, 51, 52, 53, 54, 55, 56, 57, 58, 59, 60, 61, 62, 63, 64, 65, 66, 67, 68, 69, 70, 71, 72, 73, 74, 75, 76, 77, 78, 79, 80, 81, 82, 83, 84. LON, longitude; LAT, latitude; SAT, surface air temperature.

Extended Data Table 2 | Description of the reanalyses.

Reanalysis	Time Interval Analysed	Horizontal Resolution	Reference
NCEP/NCAR Reanalysis 1	1949-2008	Global grid ($2.5^\circ \times 2.5^\circ$)	Ref. 85
Twentieth Century Reanalysis V2	1872-2010	T62 Gaussian grid ($\sim 2.0^\circ \times 2.0^\circ$)	Ref. 86
ERA Interim	1980-2011	T255 Gaussian grid ($\sim -0.75^\circ \times 0.75^\circ$)	Ref. 87
ERA40	1959-2001	T159 Gaussian grid ($\sim 1.125^\circ \times 1.125^\circ$)	Ref. 88

Data are from refs 85, 86, 87, 88. NCEP, National Centers for Environmental Prediction; NCAR, the National Center for Atmospheric Research.

Extended Data Table 3 | Description of the simulations.

Simulation*	PMIP3/CMIP5 family of experiments	Time Span	Reference
BCC-CSM1-1	past1000(r1i1p1)+historical(r1i1p1)	850-2005 CE	Ref. 89
CCSM4	past1000(r1i1p1)+continuation	850-2005 CE	Ref. 90
CSIRO-MK3L-1-2	past1000(r1i1p1)+continuation	851-2005 CE	Ref. 91 [†]
FGOALS-g1	past1000(r1i1p1)	1000-1999 CE	Ref. 92
GISS-E2-R	past1000(r1i1p121)+continuation	850-2005 CE	Ref. 93
IPSL-CM5A-LR	past1000(r1i1p1)+continuation	850-1999 CE	
MIROC-ESM	past1000(r1i1p1)+continuation	850-2005 CE	Ref. 94
MPI-ESM-P	past1000(r1i1p1)+continuation	850-2005 CE	Ref. 95

* Further information on the resolution and forcings used in the past 1,000 simulations can be found at https://wiki.lsce.ipsl.fr/pmip3/doku.php/pmip3:database:status#past1000_experiment_status_and_bc

[†]This article describes a different simulation, but specifies the differences with respect to the PMIP3 run.

Data are from refs 89, 90, 91, 92, 93, 94, 95.

Extended Data Table 4 | Principal-component (PC) contributions to the ensemble reconstructions.

Simulation	PC1	PC2	PC3	PC4	PC5
NAO _{occ}	100	98	49	11	2
NAO _{mc}	100	0	0	0	0

Extended Data Table 5 | Description of the NAO/sea-level pressure (SLP) records used for validation.

Reference	Data sources*	Regions represented	Validation period
Ref. 32	Instrumental pressure data	Eastern North Atlantic/ Europe	1781-1822 CE
Ref. 33	Instrumental, documentary and proxy data	Eastern North Atlantic/ Europe	1659-1822 CE
Ref. 34	Instrumental SLP and wind from ship logs	Eastern North Atlantic/ Europe	1751-1822 CE
Ref. 35	5 tree-ring and 2 ice cores	Morocco/Finland/Greenland	1429-1822 CE
Ref. 36	Instrumental, documentary and proxy data	Eastern North Atlantic/ Europe	1500-1822 CE
Ref. 24	367 records (tree-rings and ice cores)	Europe/Greenland/Eastern North America	1400-1822 CE
Ref. 7	1 speleothem and 1 tree-ring chronology	Scotland/Morocco	1049-1822 CE

* Only the two proxies used in ref. 7. have been included in our analysis.
 Data are from refs 7, 24, 32, 33, 34, 35, 36. ce, Common Era, equivalent to AD.

Extended Data Table 6 | The 11 largest volcanic eruptions between AD 1049 and AD 1969 in three alternative reconstructions.

Reconstruction	Reconstructed variable	List of volcanoes
Ref. 28	Global aerosol optical depth at 550 nm*	1229,1258,1286,1456,1600,1641,1674,1696,1809,1816,1884
Ref. 29	Global total stratospheric sulfate aerosol injection (in Tg) [†]	1167,1227,1258,1275,1284,1452,1600,1641,1783,1809,1815
Ref. 30	Antarctic volcanic sulfate (in kg/km ²) [‡]	1169,1229,1257,1276,1285,1344,1458,1600,1694,1809,1815

*Data from http://www1.ncdc.noaa.gov/pub/data/paleo/climate_forcing/volcanic_aerosols/crowley2013/crowley2013aod-reff.txt

†Revised version from http://climate.envsci.rutgers.edu/IVI2/IVI2TotalInjection_501-2000Version2.txt

‡Data available in the supplement of ref. 30.

Extended Data Table 7 | Eleven large volcanic eruptions common to the three alternative reconstructions.

Volcano	Country	Final selected date	Date from Ref. 28	Date from Ref. 29	Date from Ref. 30
Unknown		1229	1229	1227	1229
Samalas	Indonesia	1257*	1258	1258	1257
Unknown		1285	1286	1284	1285
Huaynaputina	Peru	1600[†]	1600	1600	1600
Parker	Philippines	1640[†]	1641	1641	1641
Serua	Indonesia	1693[†]	1696	1693	1694
Unknown		1809	1809	1809	1809
Tambora	Indonesia	1815[†]	1816	1815	1815
Cosiguina	Nicaragua	1835[†]	1835	1835	1834
Krakatau	Indonesia	1883[†]	1884	1883	1884
Agung	Indonesia	1963[†]	1964	1963	1963

* Date recently constrained using local deposits and historical records⁴⁷.

† Date extracted from historical observations⁴⁶.